SAND75-0087
Unlimited Release

Development of a High Velocity Solid Particle Launcher for Laboratory Erosion Studies

D. P. Aeschliman, A. J. Mulac, J. A. Guzman, R. R. Eaton, R. L. Fox

Prepared by Sandia Laboratories, Albuquerque, New Mexico 87115
and Livermore, California 94550 for the United States Energy Research
and Development Administration under Contract AT(29-1)-789

Printed March 1975

Sandia Laboratories

SF 2900 Q(7-73)

Issued by Sandia Laboratories, operated for the United States Energy Research and Development Administration by Sandia Corporation.

SAND75-0087
Unlimited Release
Printed March 1975

DEVELOPMENT OF A HIGH VELOCITY SOLID PARTICLE LAUNCHER FOR LABORATORY EROSION STUDIES

D. P. Aeschliman, A. J. Mulac, and J. A. Guzman
Experimental Aerophysics Division 5642
R. R. Eaton
Applied Fluid Mechanics Division 5644
R. L. Fox
Atomic and Fluid Physics Division 5641
Sandia Laboratories, Albuquerque, NM 87115

ABSTRACT

A solid particle launcher for laboratory erosion studies has been developed and successfully demonstrated. Performance of the launcher is predicted by a two-dimensional, time-dependent theoretical analysis to within the experimental uncertainty. The present device accelerates 100 μm diameter glass spheres to velocities of 2.1 ± 0.6 km/sec. The system is safe, reliable, and has a test repetition of about 2 shots/hour.

CONTENTS

		Page
	Abstract	1
	List of Figures	4
	Nomenclature	6
I.	Introduction	7
II.	Experiment	10
	2.1. Particle Launcher	10
	2.2. Instrumentation	14
	2.3. Operating Procedures	16
	2.4. Performance	16
III.	Analysis	21
	3.1. Geometry of the Two-Dimensional Analysis	21
	3.2. Basic Equations	22
	3.3. Boundary Conditions	23
	3.4. Initial Conditions	24
	3.5. Two-Dimensional Fluid-Dynamic Solutions	26
	3.6. Particle Acceleration	26
IV.	Conclusions	31
V.	References	32

LIST OF FIGURES

Figure		Page
1.	Schematic diagram of High Velocity Particle Launcher and associated instrumentation.	11
2.	.458 Magnum cartridge cases and Lexan piston. The white band is Teflon tape which provides a gas-tight seal during initial pressurization of the barrel with helium. Typical loads are 17 grains of Hercules HRF powder. Cartridge cases: upper right - unfired; left - fired.	11
3.	Schematic diagram of accelerator section.	12
4.	Photograph of diassembled accelerator section.	
5.	80X photograph of nominal 100 μm glass beads on 0.5 mil Lexan film diaphragm material.	13
6.	Chopped dual-beam oscilloscope record from pressure transducers located in barrel as shown. Upper traces: Transducer outputs displayed at 200 μsec/cm. Lower traces: Same output delayed 800 μsec and displayed at 50 μsec/cm. A - Incident shock arrival at PT1; B - Incident shock arrival at PT2; C - Reflected shock arrival at PT2; D - Reflected shock arrival at PT1. Incident shock speed = 2.1 mm/μsec.	15
7.	Typical 10X photograph of 2024-T3 Aluminum target after impact by 100 μm glass spheres. Irregular craters are presumably due to impact by diaphragm material.	18
8.	Histogram of number of impact craters vs. ratio of crater depth (from plane of target surface), p, to crater diameter (in plane of target surface), d. Data shown are from five targets impacted at identical accelerator conditions.	20

LIST OF FIGURES (cont)

Figure		Page
9.	Histogram of number of particles vs. particle diameter. Reduced peak near 100 μm is apparently due to prior culling of the particle batch to remove particles in the 95-100 μm diameter range.	
10.	Geometrical model for two-dimensional flow analysis.	22
11.	Gas velocity distribution inside accelerator section for various times (Case I). Shock initially at point shown at time t = 0. Arrows indicate positions of reflected and transmitted shocks at t = 90 μsec. Incident shock speed is 2.1 mm/μsec.	27
12.	Pressure distribution inside accelerator section for various times (Case I). Conditions same as for Fig. 11. P_{II} is the initial pressure in Region 2 of Fig. 11.	
13.	Calculated velocity of 100 μm glass sphere as a function of time (Case I). C_D is an effective drag coefficient for the sphere, time defined as in Fig. 11.	28
14.	Gas velocity as a function of position in accelerator for various times, as defined in Fig. 11 (Case II). Incident shock speed is 2.1 mm/μsec. Negative velocity represents flow toward gun breech.	29
15.	Pressure distribution inside accelerator section for various times (Case II). Conditions same as for Fig. 14.	
16.	Calculated velocity of 100 μm glass sphere as a function of time (Case II).	30

NOMENCLATURE

English

C_D	drag coefficient
d	impact crater diameter, measured in plane of original surface
E	energy
h	enthalpy, energy/unit mass
M	Mach number
P	pressure
p	penetration depth, measured from plane of original surface
r	radius
t	time
u	velocity component in r-direction
w	velocity component in θ-direction

Greek

γ	gas specific heat ratio
θ	angular displacement from axis, spherical coordinates
ρ	mass density

Subscripts

p	particle, piston
r	radial, reflected
s	shock
1	Region 1
2	Region 2

DEVELOPMENT OF A HIGH VELOCITY SOLID PARTICLE ACCELERATOR FOR LABORATORY EROSION STUDIES

I. Introduction

Reentry vehicle (RV) heat shield erosion due to high-speed impacts by solid particulate matter is potentially a serious problem. The source of such material might be natural atmospheric ice, snow, or dust, or dust convected into the atmosphere following a low-altitude nuclear burst. This problem may be of concern even at erosion levels well below those required for actual vehicle destruction, since variations in vehicle drag or symmetry might produce guidance errors that are unacceptably large.

RV erosion from rain, ice, and snow has been examined experimentally for a number of representative nosetip and heat shield designs in the SAMS* program. Nosetips instrumented to provide erosion rate data have been launched using high performance (up to 3.4 km/sec at 6 km altitude) Sandia designed rocket systems through active storms, and recovered. Storm data were provided by both ground-based radar and by local sampling. Although the erosion environment is usually not very well characterized, these tests have provide much useful data.[1-4] The SAMS tests, however, are quite expensive (> $100K/shot), they are inconvenient in that scheduling depends on the vagaries of the weather, and in-depth nosetip temperature and composition profiles generally differ from those of an RV following atmospheric entry.

*Sandia-Air Force Materials Study

Because of these reasons there is a need for an inexpensive laboratory testing method (especially one that could be combined with a programmed sample preheating capability). Several facilities exist that eliminate one or more of the problems associated with the rocket flight tests.

The rocket sled test track at Holloman AFB can be used at up to ~ 2km/sec with artificial erosion environments. (See for example, Ref. 5). Aside from the reduced performance capability, these tests are also expensive (≥ $50K/shot), and a pre-heat capability is not presently available.

Light gas gun launch facilities exist at Arnold Engineering Development Center (AEDC),[6] Naval Ordnance Laboratory (NOL),[7] Avco,[8] and General Motors Defense Research Labs.[9] Sample nosetips of 1.2 - 5.0 cm diameter can be launched through artificial erosion fields at velocities up to 6 km/sec. Because samples are not generally recoverable, sophisticated in-flight range instrumentation is required. Facility investments run $1-10 M, with per shot costs of $5-10K. The feasibility of preheating light gas gun launched samples has recently been demonstrated at NOL.[10]

In contrast to the above techniques, methods exist in which a stationary sample is impacted by moving particulate. Particles possessing an electrical charge have been accelerated to speeds of 5-10 km/sec using a high-voltage accelerator, as demonstrated by Friichtenicht[11] and Arnold, et. al.[12] Because of charge-to-mass ratio limitations, maximum particle diameters are ~ 1 μm . Facility costs are ~ $1-10 M.

Scully, et. al.,[13] have used an "electro-thermal" accelerator to launch spheres up to 50 μm diameter to speeds of 5-20 km/sec. In this

technique, hot gas outflow from a large capacitive discharge is used to accelerate the particles by entrainment. The major disadvantage of the method is that the particles suffer rather severe ablation in the process.

A similar difficulty was observed by Mirtich and Mark[14] who used a shock tube flow to entrain particles to high speeds ($\geq$ 3 km/sec). More recently, AEDC has attempted to seed an arc-heated wind tunnel with particulate.[6] However, achievable velocities are low (1-2 km/sec), and particle ablation may be serious. A similar method is described by Lorenz.[15]

For one or more reasons, none of the methods described possess all of the desired characteristics. The solid particle accelerator described in this report utilizes entrainment as the accelerating mechanism, but does so with dense, relatively cold gas so as to minimize the particle ablation problem. In addition, it is readily adaptable to the Sandia 2-MW plasmajet so as to permit testing of materials at typical heat shield ablation temperatures. Total facility development costs are well under \$100K; anticipated per-shot costs are $\lesssim$ \$0.1K.

Details of the system are presented in Section II. In Section III a theoretical analysis of the particle accelerator performance is presented. Conclusions are presented in Section IV.

II. Experiment

In this section, the experimental apparatus and operation are described.

2.1 Particle Launcher

The particle launcher consists of a smooth bore gun, accelerator section, evacuated test section, and a target. A block diagram of the system is shown in Fig. 1. A smooth-bore .458 cal (1.163 cm I.D.) gun with a standard Remington Model 700 action, is mated to the accelerator section at the gun muzzle. High pressure helium (> 10 atm) in the barrel is compressed by a supersonic piston fired from a standard .458 magnum cartridge case. The pistons (1.168 cm dia. x 1.27 cm long) are made of Lexan plastic because of its extremely high impact resistance. The cartridge is wrapped with a band of Teflon tape, shown in Fig. 2, that provides a gas seal for the high pressure helium during the initial pressurization.

The shock wave generated by the piston in the gun section enters the convergent nozzle section of the accelerator, shown schematically in Fig. 3. Fig. 4 is a photograph of the disassembled accelerator. Particles attached to a thin diaphragm, located at the throat of the converging-diverging accelerator section are entrained in expanding, supersonic helium following diaphragm rupture, and swept downstream through the test section.

The diaphragm material is .00127 cm thick aluminized Lexan plastic film. The diaphragms are cut so as to overlap an "O" ring in the nozzle assembly, thus providing an adequate seal between the high-pressure barrel and the test section. Static rupture pressure for the diaphragms exceeds 20 atm.

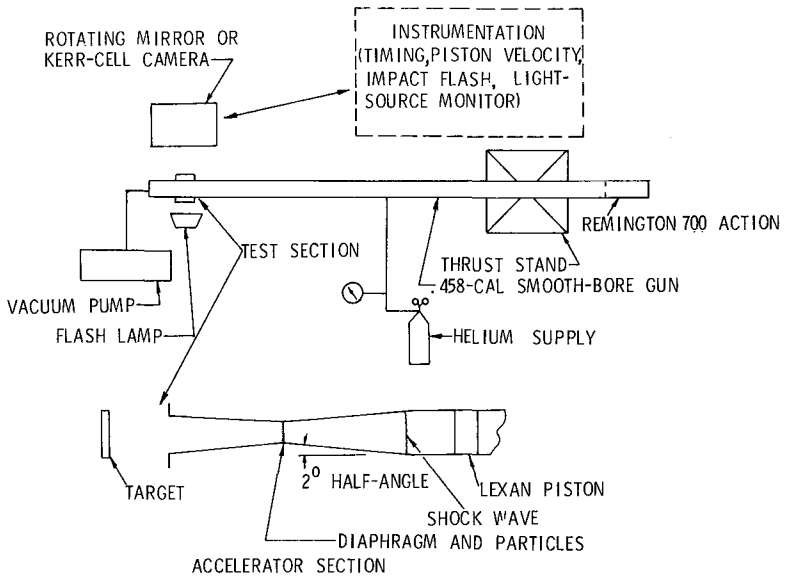

Fig. 1. Schematic diagram of High Velocity Particle Launcher and associated instrumentation.

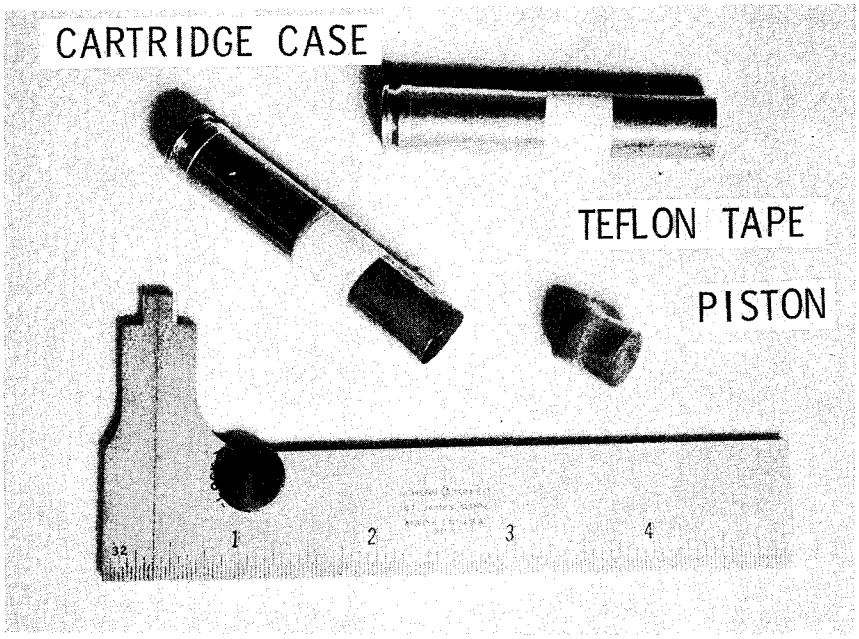

Fig. 2. .458 Magnum cartridge cases and Lexan piston. The white band is Teflon tape which provides a gas-tight seal during initial pressurization of the barrel with helium. Typical loads are 17 grains of Hercules HRF powder. Cartridge cases: upper right - unfired; left - fired.

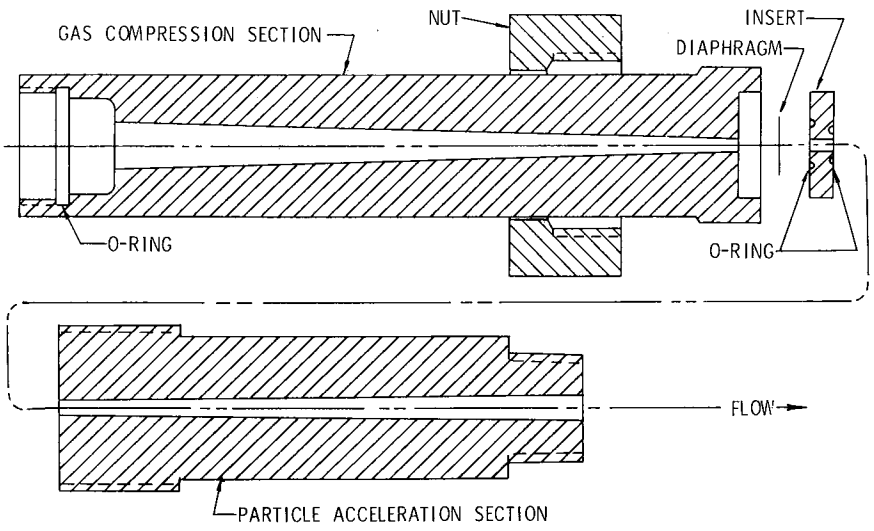

Fig. 3. Schematic diagram of accelerator section.

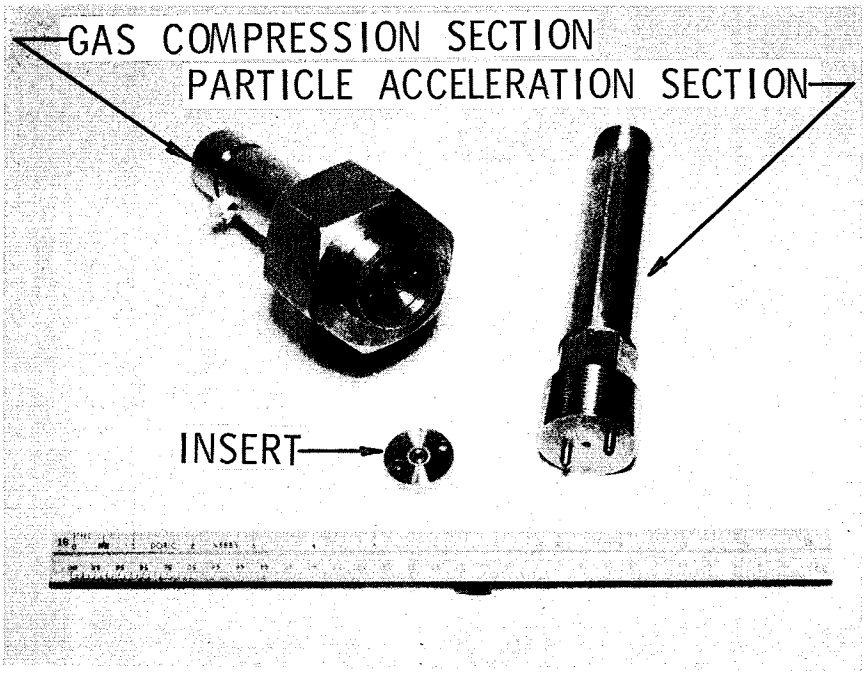

Fig. 4. Photograph of diassembled accelerator section.

The projectiles currently in use are 100 μm glass beads supplied by the 3M Company. The specific gravity of the beads is about 2.6. Figure 5 is an 80-X photograph of the beads on a diaphragm; a very thin coat of vacuum grease is used to adhere the particles to the diaphragm.

Two different test sections were used. The first is a 2.7 cm I.D. cylindrical chamber with 1.8 cm O.D. glass windows located 5 cm downstream of the nozzle exit. Target samples are located at the window aperture. The cylinder is evacuable to 0.3 torr.

The second test chamber is a 38 cm W. X 38 cm H. X 53 cm L. steel reinforced box made of clear acrylic plastic. The chamber has 14 cm x 20 cm plate glass windows on opposite sides, and is evacuable to about 5 torr.

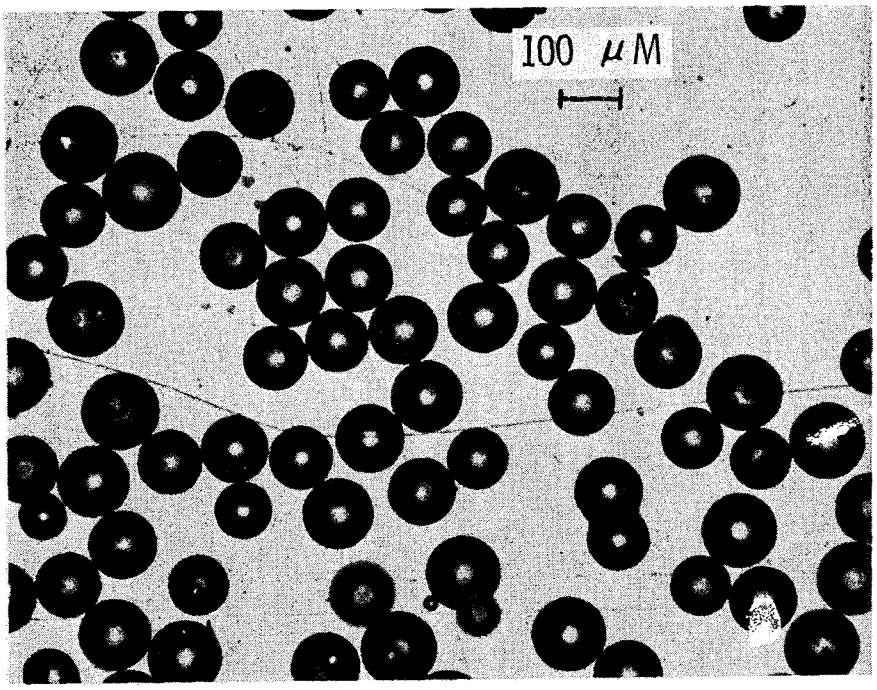

Fig. 5. 80X photograph of nominal 100 μm glass beads on 0.5 mil Lexan film diaphragm material.

2.2 Instrumentation

During each firing, the following variables are monitored: the speeds of the incident shock preceding the piston, and the shock reflected from the diaphragm; the time from cartridge detonation to shock arrival at the muzzle; and total light emitted in the test section due to interaction between the particles and the ambient test section air.

The shock speeds are determined using two Susquehanna pressure transducers, mounted 7.6 cm apart in the barrel. A typical oscilloscope record is shown in Fig. 6. The early time signal was provided by a piezoelectric crystal gage mounted on the outside of the gun breech wall. The optical output records (not shown) were obtained with a silicon diode detector whose spectral response peaked at about 0.9 μm.

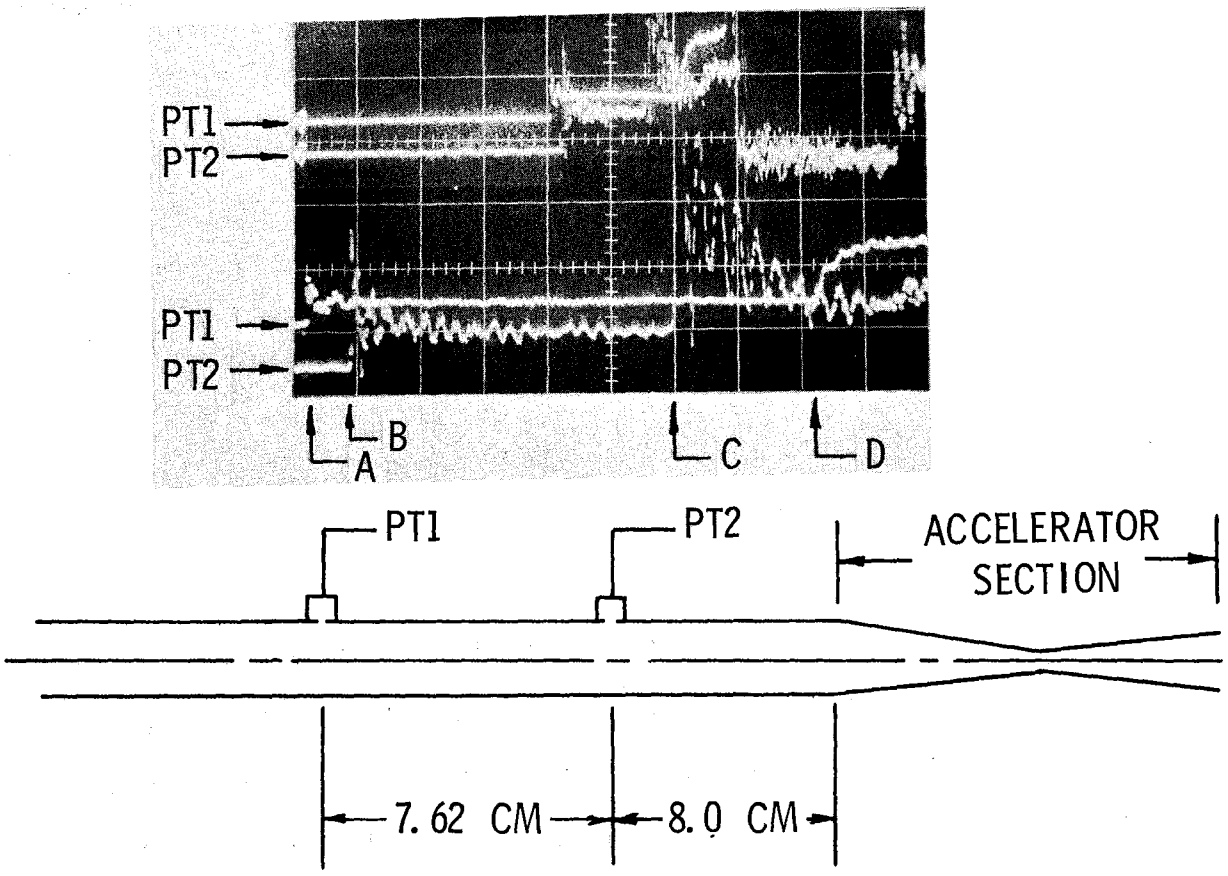

Fig. 6. Chopped dual-beam oscilloscope record from pressure transducers located in barrel as shown. Upper traces: Transducer outputs displayed at 200 μsec/cm. Lower traces: Same output delayed 800 μsec and displayed at 50 μsec/cm. A - Incident shock arrival at PT1; B - Incident shock arrival at PT2; C - Reflected shock arrival at PT2; D - Reflected shock arrival at PT1. Incident shock speed = 2.1 mm/μsec.

2.3 Operating Procedures

The operating procedure is typically as follows: the entire system is cleaned; a greased diaphragm inserted and the nozzle section assembled; particles are poured in the nozzle exit and the excess poured out (this assures an essentially uniform distribution of particles on the diaphragm); a target is installed; the accelerator section is mated to the gun; a loaded cartridge is inserted, the bolt closed, and made safe; the test chamber and the barrel are evacuated; the barrel is isolated from the vacuum pump and backfilled with helium up to 14 atm; instrumentation is readied; the safety is released and the gun is hand-fired. The turn-around time is approximately 30 minutes.

2.4 Performance

The performance of the accelerator depends on the initial conditions. Initial helium pressure was varied from 10 to 14 atm. Cartridge powder loading is selected such that the piston stops just short of the converging section. A suitable load yielding highly reproducible performance has proven to be 17 to 18 grains of Hercules HRF (High Rate Flake, a fast-burning, pre-production rifle powder). Heavier loads lodged the piston in the converging section with no apparent improvement in performance; lighter loads significantly reduced the piston velocity.

Piston velocities are deduced from the incident shock-speed records. Typically, shock speeds are 2.0 km/sec, yielding piston velocities of $\sim$ 1.1 km/sec. This latter value represents the piston speed shortly before it comes to rest; piston deceleration is due to the high helium pressure on the piston front-face, decreasing piston driving pressure with distance from the breech, and friction in the barrel. The range of inci-

dent and reflected shock velocities for different initial conditions, and the variability in these parameters for fixed initial conditions, are shown in Table I.

Particle velocities are determined from the depth of the craters produced by impact into a known target material. For this purpose, a 100X microscope with a vertical traverse micrometer is used. Figure 7 shows a 10X photograph of the craters in an aluminum target. The small, more uniform craters are due to particle impact by 100 μm (nominal) glass particles. The larger, more irregular craters are apparently the result of diaphragm debris impact. Strands of diaphragm material were found in many of the larger craters.

Forty-eight craters from 5 targets were examined. A histogram of the crater depth is shown in Fig. 8. The center of the broad peak in this distribution corresponds to a particle velocity of 1.5 - 2.7 km/sec (0.5 - 0.9 x 10^4 fps) depending on which of the available velocity-crater depth correlations[16-18] is used.

However, direct comparison of the present results to available experimental data (as opposed to correlations based on those data) yields particle velocities at the higher end of the indicated range. Using the granite projectile (ρ_p = 2.6 g/cc) / 6061-T6 aluminum target data of Zimmerman,[19] a most probable particle velocity of 2.4 km/sec is obtained for p/d = 0.9. (p = penetration depth from original surface, d = crater diameter in plane of the surface). This estimate also agrees with the data of Maiden, et al.,[20] obtained using 2024-T3 targets, and of Collins and Kinard,[21] using 24ST Al targets. It is of interest to note that tempered Al targets yield p/d data[19,20] that agree quite well ($\approx \pm$ 10%); however, annealed aluminum targets yield p/d's about a factor of 2 higher[21] for the same velocity. Apparently,

TABLE I

Test	U_p	U_s	U_r	Gas	P_1	Powder Load
	(mm/μs)	(mm/μs)	(mm/μs)		(10^5 Pa)	(Grains)
1	1.0	1.27		N_2	9.1 *	17
2		1.90	1.17	He	9.1	17
3		1.90	0.7	He	11.4	18
4	1.1	2.01	1.05	He	11.4	18
5		1.91	1.19	He	11.4	18

*The gun was not evacuated for these cases; indicated pressure includes 1 atm ambient air.

Fig. 7. Typical 10X photograph of 2024-T3 Aluminum target after impact by 100 μm glass spheres. Irregular craters are presumably due to impact by diaphragm material.

strength effects in aluminum are quite important at velocities < 3 km/sec, as noted by Herrmann and Jones.[18]

The large variability in p/d evident in Fig. 8 is not fully explained. A random variation of ± 20% is traceable to the observed ± 30% variation in glass sphere diameter indicated in Fig. 9* and uncertainties of 5-10% are due to errors in the measurement of p and d. Other potential sources of scatter in p/d are misidentification of debris craters for sphere craters, anomalous particles (double or triple-fused, of which 5% fall in this category) and particle fragmentation prior to impact. Also, gradients in particle velocity may exist as functions of time after diaphragm rupture, and radial and axial position in the helium effluent.

In addition to the crater depth measurements, several other particle velocity measurement techniques were attempted. These included: high speed framing camera pictures; light flash intensity from targets; and light scattering using a multiple-beam laser velocimeter. All of these approaches failed to provide definitive velocity data due to one or more of the following difficulties: lack of optical resolution; poor optical contrast ratio; and the possible presence of debris mixed with the particles. Unless this uncertainty in velocity can be reduced, the accelerator may be restricted to application as a material screening device.

*The maximum variation of particle velocity u_p with particle radius r_p is proportional to $\frac{1}{r_p}$; and, $(p/d) \sim u_p^{2/3}$.

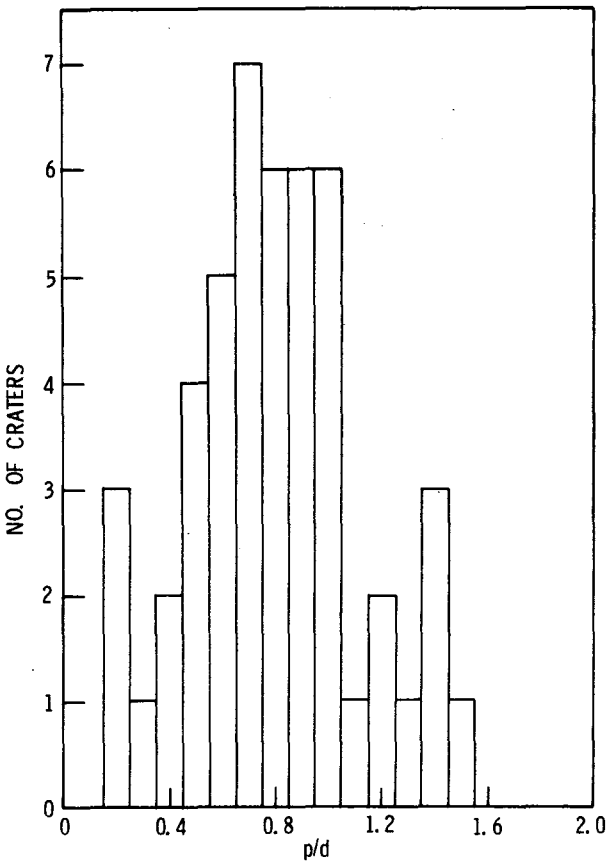

Fig. 8. Histogram of number of impact craters vs. ratio of crater depth (from plane of target surface), p, to crater diameter (in plane of target surface), d. Data shown are from five targets impacted at identical accelerator conditions.

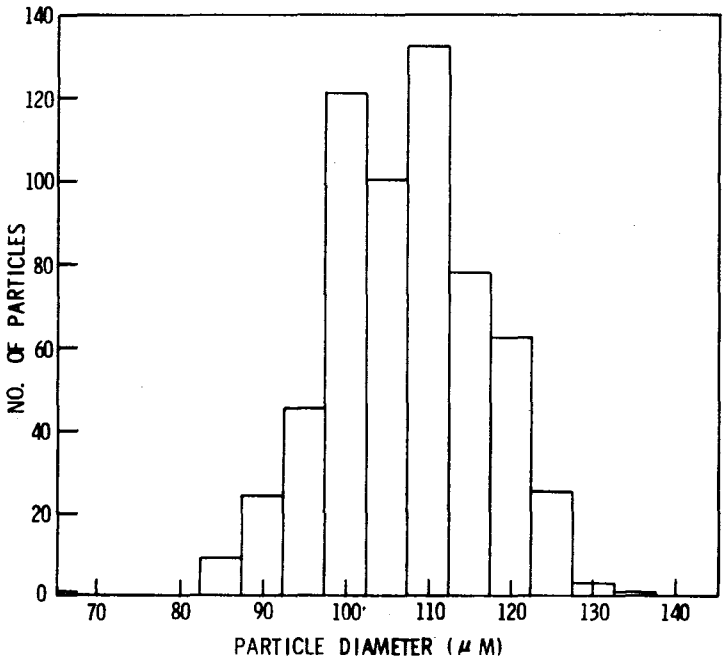

Fig. 9. Histogram of number of particles vs. particle diameter. Reduced peak near 100μm is apparently due to prior culling of the particle batch to remove particles in the 95-100 μm diameter range.

III. Analysis

A one-dimensional model was first developed to predict the performance of the accelerator. This model included the area expansion of the downstream section of the apparatus and assumed a steady reservoir condition corresponding to the shock-heated gas in the straight section of the gun. The results of this calculation substantially underpredicted the measured performance. An unsteady two-dimensional analysis which treats the entire geometry is presented below. This model allows for simultaneous gas and particle acceleration.

3.1 Geometry of the Two-Dimensional Analysis

The design geometry of the particle accelerator was decomposed into two separate spherical coordinate systems as demonstrated in Fig. 10. The decomposition of the accelerator in this manner aids in the calculation by placing the walls along radial lines of the spherical coordinate systems. The individual sections have the proper form for solution using methods previously developed for calculation of the flow in the line-of-sight pipe in underground nuclear experiments (code 2 D/LOS).[22] The solution can thus be carried out by holding the given fluid parameters constant at Location A in Fig. 10, given some initial values in Region 2 with a reflecting boundary at the diaphragm location, B_1. The development and progress of the shock front through the accelerator is calculated by 2 D/LOS. The arrival of the shock at point B_1 results in a characteristic increase in the local pressure. The pressure at point B_1 eventually becomes sufficient to break the diaphragm, at which time the boundary conditions at this location are changed from a reflecting wall to a flow-through orifice.

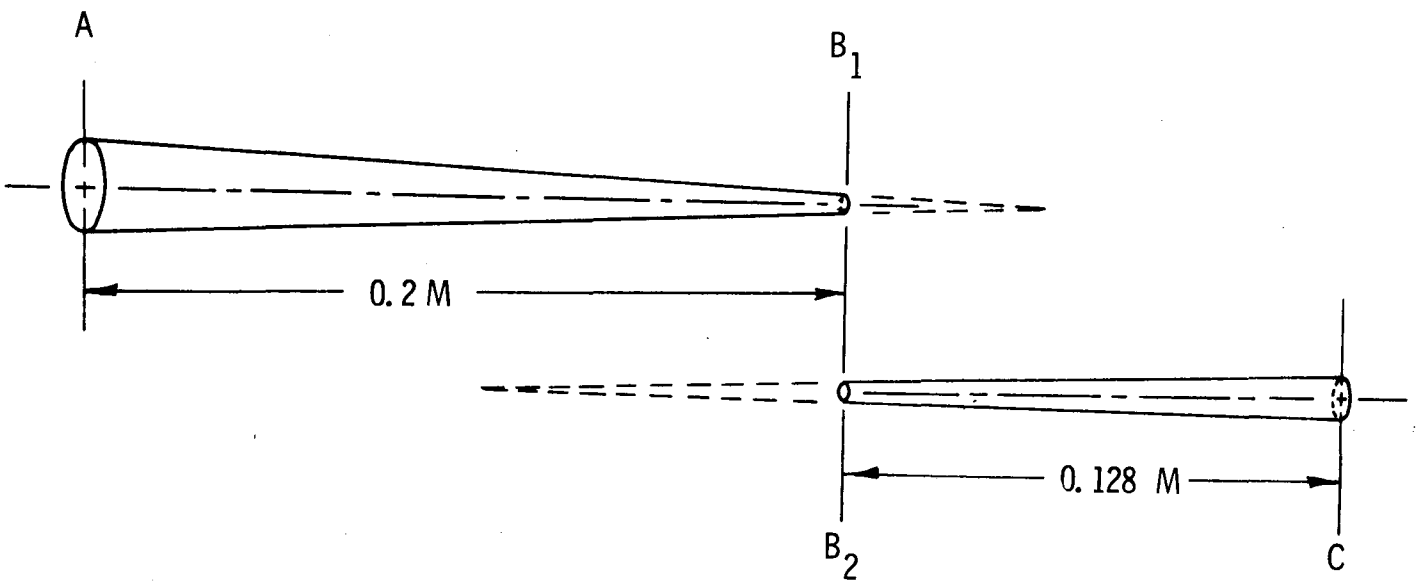

Fig. 10. Geometrical model for two-dimensional flow analysis.

Simultaneous to the change in the boundary condition at point B_1, a separate solution for Region 3 is initiated. The solution for Region 3 is obtained from a 2 D/LOS code which used the instantaneous fluid parameters at B_1 for the upstream time-dependent values at B_2 with a given initial fluid characteristic in the remaining portions of the accelerator.

After a specified time the conditions at Point A are changed from a constant to reflecting boundary in order to simulate the stopping of the driver piston. In this manner the shock is allowed to effectively propagate from Region 2 through Region 3 and out of the accelerator via flow-through boundary conditions at point C. Consequently, the high-velocity fluid in Region 3 accelerates the spherical particles initially located on the separating diaphragm.

3.2 Basic Equations

The system of fluid equations for the spherical geometry and the method of solution are discussed in detail in Ref. 22 and will only be briefly reviewed here.

The partial differential equations considered are the time-dependent Euler equations written in axisymmetric spherical coordinates.[23] These equations are:

Continuity:

$$\frac{\partial}{\partial t}(\rho r^2 \sin\theta) + \frac{\partial}{\partial r}(\rho u r^2 \sin\theta) + \frac{\partial}{\partial \theta}(\rho w r \sin\theta) = 0 ,$$

r-Momentum:

$$\frac{\partial}{\partial t}(\rho u r^2 \sin\theta) + \frac{\partial}{\partial r}[(\rho u^2 + P) r^2 \sin\theta] + \frac{\partial}{\partial \theta}(\rho u w r \sin\theta)$$

$$= (2P + \rho w^2) r \sin\theta ,$$

θ-Momentum:

$$\frac{\partial}{\partial t}(\rho w r^2 \sin\theta) + \frac{\partial}{\partial r}(\rho u w r^2 \sin\theta) + \frac{\partial}{\partial \theta}[(\rho w^2 + P) r \sin\theta]$$

$$= rP\cos\theta - \rho u w r \sin\theta ,$$

Energy:

$$\frac{\partial}{\partial t}(E r^2 \sin\theta) + \frac{\partial}{\partial r}[u(E + P) r^2 \sin\theta] + \frac{\partial}{\partial \theta}[w(E + P) r \sin\theta] = 0 .$$

3.3 Boundary Conditions

Before the partial differential equations can be solved, conditions at the boundaries of the region of interest must be specified. These include the centerline, accelerator extremities, and walls.

The accelerator inlet conditions are specified and the properties of the exit are given zero slopes along r. The accelerator centerline is a line of symmetry. The converging and diverging walls are considered surfaces of symmetry. The properties are thus reflected about these

boundaries. On the centerline the w-velocity vanishes identically, thus eliminating the normal momentum equation. The indeterminate terms in the remaining equations have the general form

$$\frac{1}{\sin\theta}\frac{\partial}{\partial\theta}(A \sin\theta)$$

which reduces to $2\frac{\partial A}{\partial\theta}$ for $\theta \to 0$.

These equations were coded for use on the CDC 6600 computer. Approximately 10 minutes of computer time are required to run one case which contains two hundred evenly distributed mesh points along the accelerator centerline.

3.4 Initial Conditions

The gas conditions required to initiate the calculation were experimentally determined from pre-shot temperature and pressure measurements in addition to the shock velocity in Region 1 as determined using pressure transducers. The remainder of the conditions required by the code were obtained from simultaneous solutions to the following equations:

Mach number:

$$M_s = \frac{u_s}{\sqrt{\gamma \frac{P_2}{\rho_2}}} ;$$

Momentum:

$$P_r = 1 + \gamma M_s^2 \left(1 - \frac{1}{\rho_r}\right) ;$$

Energy:

$$h_r = 1 + \frac{(\gamma - 1)}{2} M_s^2 \left(1 - \frac{1}{\rho_r^2}\right) ; \text{ and}$$

Equation of state:

$$\rho_r = \frac{P_r}{h_r} \quad .$$

Pressure, density, and energy are nondimensionalized with their respective values in Region 2. Using this information, the velocity, density, pressure, and energy were determined (Table II) for two cases of interest. Case I is the set of initial conditions which most closely simulates the actual experimental test. Case II models the flow for reduced initial pressure and increased shock speed, conditions which appear to be achievable experimentally.

TABLE II

Initial Conditions

CASE		Region I	Region II	Region III
I	P	4.95×10^5	11.4×10^5	4.0×10^2 (Pa)
	ρ	4.05	1.84	6.6×10^{-4} (Kg/m^3)
	T	5.89×10^2	2.98×10^2	289 (K)
	U_p	1.065×10^3	0.0	0.0 (m/s)
II	P	5.08×10^6	9.1×10^5	4.0×10^2 (Pa)
	ρ	3.66	1.51	6.6×10^{-4} (Kg/m^3)
	T	6.67×10^2	2.89×10^2	2.89×10^2 (K)
	U_p	1.266×10^3	0.0	0.0 (m/s)

3.5 Two-Dimensional Fluid-Dynamic Solutions

The progress of the fluid dynamic shock through the converging and diverging section of the particle accelerator is shown in Fig. 11 for Case I. At a time, 90 μs after the solution commences, the diaphragm separating the two sections has broken and the shock is moving into the diverging region. After 105 μs the shock front is leaving the end of the accelerator and a weak backward-moving shock is progressing from the throat location. The backward-moving shock is reflected from boundary to boundary in the converging region with a loss of strength with each reflection at the diaphragm orifice. Each collision of the initially backward-moving shock with the diaphragm orifice results in a weak pulse propagating through the diverging section. The pressure profiles which correspond to the velocity profiles presented in Fig. 11 are shown in Fig. 12.

The velocity of the backward-moving shock was experimentally measured as it passed through Region I. The results varied from 0.07 cm/μs to 0.12 cm/μs. The average calculated velocity of this shock in Region II as shown in Fig. 11 was found to be 0.18 cm/μs. The average velocity of the reflected shock would be expected to be greater in Region II than Region I due to the characteristic loss of shock strength in a diverging channel.

3.6 Particle Acceleration

The particulate matter in the form of $\sim$ 100 μm diameter spheres is initially attached to the diaphragm separating the two sections of the accelerator. When the pressure differential across the diaphragm is sufficient to cause rupture, the spheres are entrained into the moving gas stream. The numerical simulation models the entrainment by coupling the particle motion and the fluid dynamics through an effective drag coefficient. The drag coefficient, C_D, for a sphere varies from 0.2

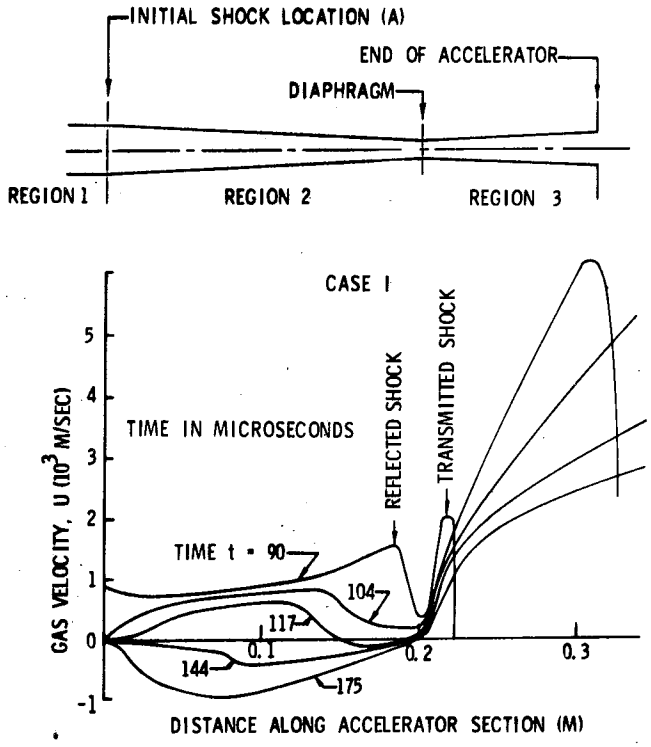

Fig. 11. Gas velocity distribution inside accelerator section for various times (Case I). Shock initially at point shown at time t = 0. Arrows indicate positions of reflected and transmitted shocks at t = 90 μsec. Incident shock speed is 2.1 mm/μsec.

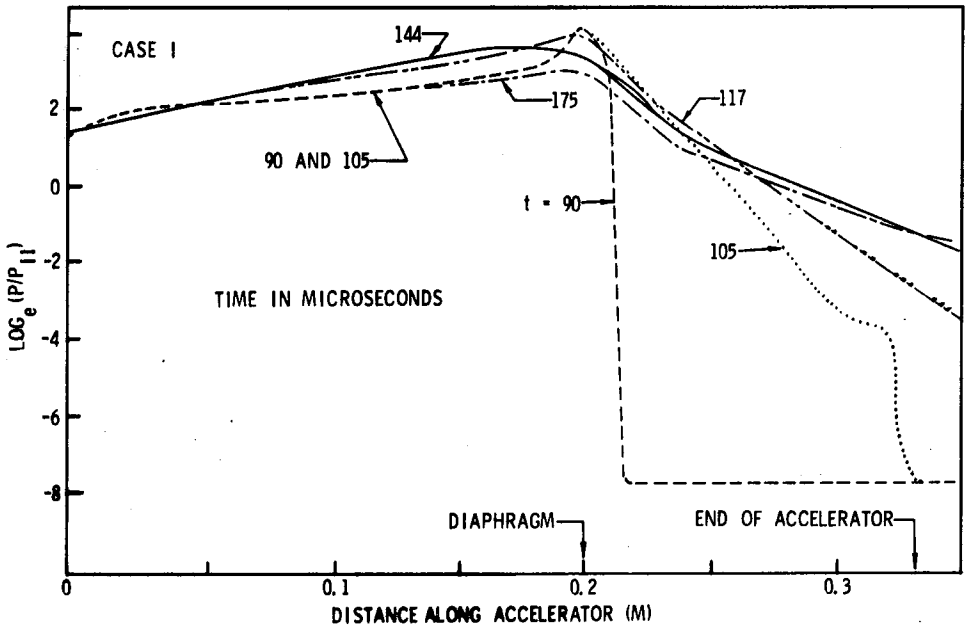

Fig. 12. Pressure distribution inside accelerator section for various times (Case I). Conditions same as for Fig. 11. P_{II} is the initial pressure in Region 2 of Fig. 11.

to 1 depending on the Reynolds number of the flow and is typically about 0.5 for fully developed turbulent flow and 1.0 for laminar flow.

The values of C_D used in the program, held constant for a given calculation, were parametrically varied from 0.25 to 1.0 for Case I. The resulting time evolution of the particle velocity due to fluid-particle interaction is shown in Fig. 13. For the above range of C_D, the calculated velocity of the particles exiting the accelerator is predicted to vary between 1.7 km/sec and 2.8 km/sec, in reasonable agreement with particle velocities of 2.1 ± 0.6 km/sec based on impact crater measurements.

The Case II results are shown in Figs. 14, 15, and 16. These results indicate that higher shock velocity and lower initial pressure combine to increase the accelerator performance.

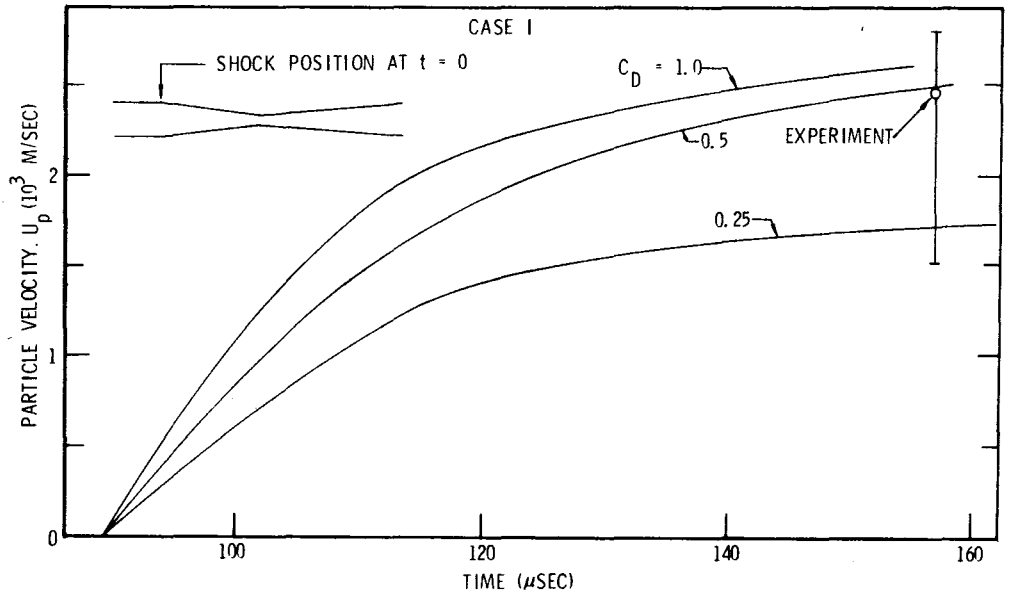

Fig. 13. Calculated velocity of 100 μm glasssphere as a function of time (Case I). C_D is an effective drag coefficient for the sphere, time defined as in Fig. 11.

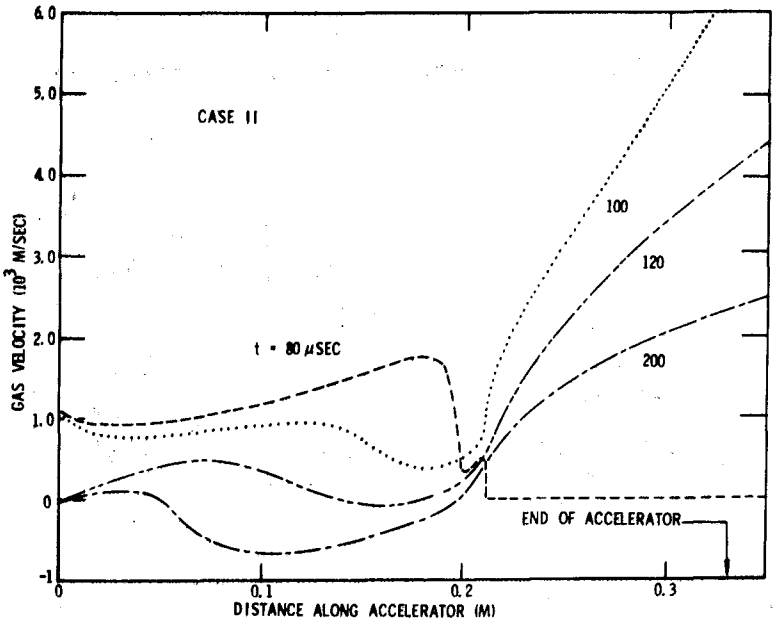

Fig. 14. Gas velocity as a function of position in accelerator for various times, as defined in Fig. 11 (Case II). Incident shock speed is 2.1 mm/ sec. Negative velocity represents flow toward gun breech.

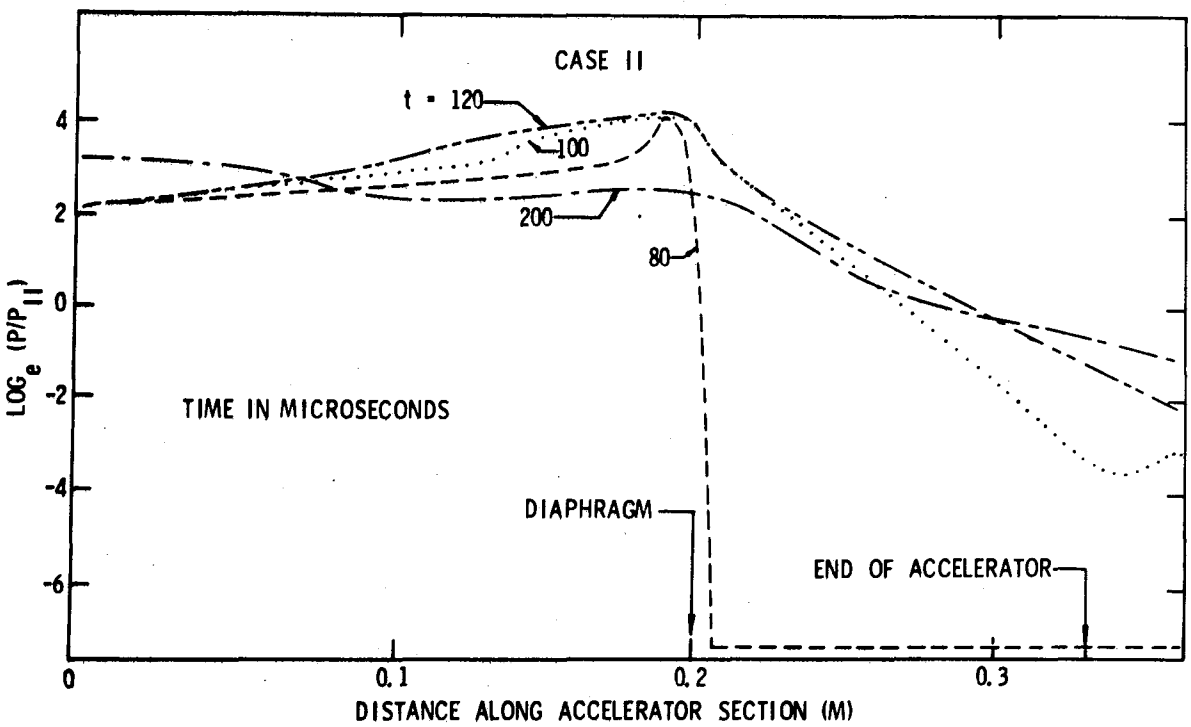

Fig. 15. Pressure distribution inside accelerator section for various times (Case II). Conditions same as for Fig. 14.

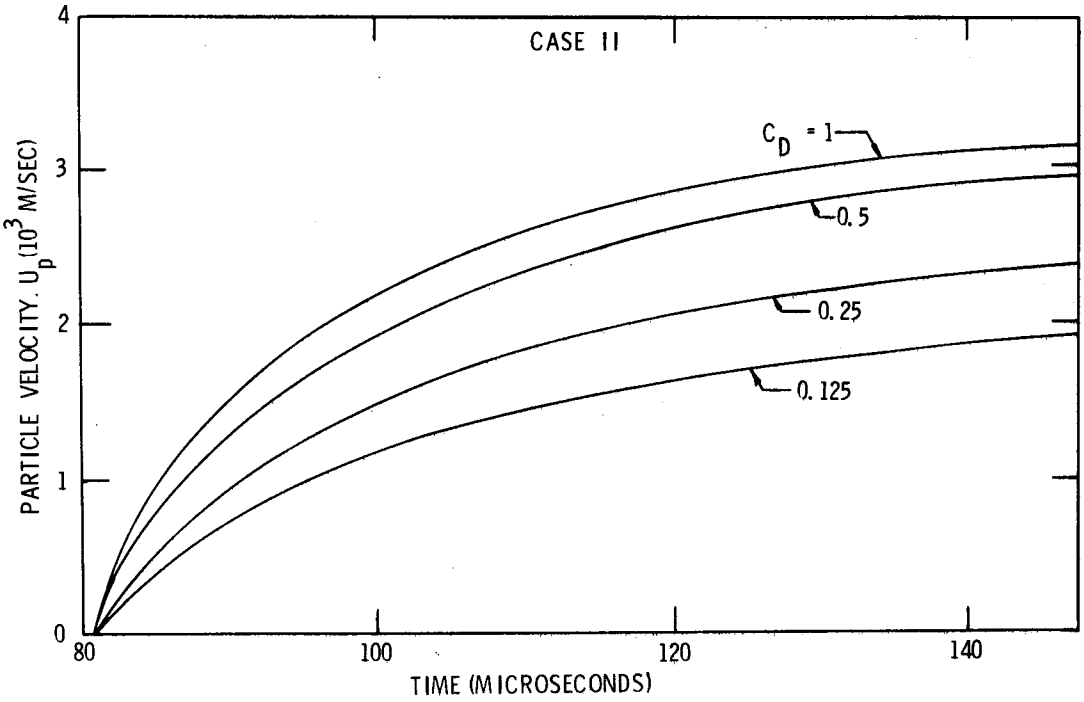

Fig. 16. Calculated velocity of 100 μm glass sphere as a function of time (Case II).

IV. CONCLUSIONS

A simple, reliable light-gas-gun particle launcher has been developed for laboratory erosion studies. The system is inexpensive to operate (< $100/shot) and is capable of 30 minute turn around time. Experimental performance is reproducible and is in substantial agreement with numerical solutions of a reasonably complete theoretical model.

Velocities of 100 μm glass spheres are observed to be 2.1 ± 0.6 km/sec, with a most probable velocity of 2.4 km/sec, and are thus on the lower end of the range of interest in reentry-vehicle erosion studies. However, additional theoretical solutions indicate that the performance can be upgraded without extensive system modification.

The large uncertainty in the velocity, and the presence of debris material in the particle stream may limit application of the launcher to qualitative erosion - resistance screening tests (i.e., on a comparative basis only). However, the relatively high test frequency and low per-shot cost, and the ability to operate in the laboratory should make the system valuable in that capacity.

V. References

1. J. K. Cole, SAMS Program Test Plan, SC-DR-70-850, Sandia Laboratories, Albuquerque, New Mexico, December 1970.

2. J. K. Cole and E. D. Robinett, Jr., Test Report for SAMS Rain Erosion Flights I and II, SC-DR-71-0649, Sandia Laboratories, Albuquerque, New Mexico, December 1971. (SDI)

3. J. K. Cole, H. W. Church, B. W. Marshall, and L. R. Rollstin, Test Report for SAMS Rain Erosion Flights 3, 4, and 5, SLA-73-0565, Sandia Laboratories, Albuquerque, New Mexico, 1973. (SNSI)

4. J. K. Cole, H. W. Church, and L. R. Rollstin, Test Report for SAMS Rain Erosion Flights 6, 7, and 8, SLA-73-0813, Sandia Laboratories, Albuquerque, New Mexico, February 1974. (SNSI)

5. K. M. Jacobs, Rain Erosion Sled Tests Final Report. AVMSD-0095-69-RR, Aerospace Corporation, February, 1969.

6. Anonymous, Utilization of the 100-ft AEDC Aeroballistic Range G for Erosion Testing, Unpublished facility description, ARO, Inc. Tullahoma, Tennessee.

7. K. R. Gastrock and N. W. Sheetz, Jr., Interim Data Report: ABRES Aggravated Erosion Program (U), Naval Ordnance Laboratory, White Oak, Maryland, 25 May 1973 (SNSI)

8. W. G. Reinecke, W. L. McKay, and S. J. Burns, Erosion Behavior of Advanced Materials Subject to High Speed Rain and Dust Impact (U), AVSD-0396-71-CR, Avco Systems Division, Wilmington, Massachusetts, August, 1971.

9. J. W. Gehring and C. Kligman, An Experimental Feasibility Study Defining Dust Cloud Interaction, TR-67-47, General Motors Defense Research Laboratories, Santa Barbara, California, September 1967.

10. Carson Lyons, Naval Ordnance Laboratory, Private Communication.

11. J. F. Friichtenicht, Two-Million Volt Electrostatic Accelerator for Hypervelocity Research, Review of Scientific Instruments, Vol. 33, No. 2, February 1962, pp 209-212.

12. K. W. Arnold, R. B. Britton, R. N. Cheever, A. S. Denholm, S. V. Nablo, and P. R. Wiederhold, A Preliminary Design Study of a Microparticle Accelerator, Final Report, NASA Contract NAS 2-1873, Ion Physics Corporation, April 1964.

13. C. N. Scully, E. A. Escallier, F. D. Rosen, and J. D. O'Keefe, Electrothermal Gun for Hypervelocity Ballistics Research, SID Report No. 64-1156, North American Aviation, Inc., 17 November, 1964.

14. M. J. Mirtich and H. Mark, Feasibility of Accelerating Micron-Size Particles in Shock-Tube Flows for Hypervelocity Degradation of Reflective Surfaces, NASA TN D-3187, January 1966.

15. G. C. Lorenz, Simulation of the Erosive Effects of Multiple Particle Impacts in Hypersonic Flow, J. Spacecraft and Rockets, Vol. 7, No. 2, February 1970, pp. 119-125.

16. J. L. Summers and A. C. Charters, High Speed Impact of Metal Projectiles in Targets of Various Materials, Proceedings of the Third Symposium on Hypervelocity Impact, Vol. 1, February 1969, pp. 101-113.

17. E. P. Bruce, Review and Analysis of High Velocity Impact Data, Proceedings of the Fifth Symposium on Hypervelocity Impact, Vol. 1, Part 2, April 1962, pp. 439-474.

18. W. Herrmann and A. H. Jones, Survey of Hypervelocity Impact Information, A.S.R.L. Report No. 99-1, Massachusetts Institute of Technology, Cambridge, Massachusetts, September 1961.

19. A. W. Zimmerman, Study of Liquid and Solid Particle Impacts, TRW-17286-6001-RO-00, TRW Systems, Redondo Beach, California, August 1971.

20. C. J. Maiden, J. Charest, and H. P. Tardiff, An Investigation of Spalling and Crater Formation by Hypervelocity Projectiles, Fourth Hypervelocity Impact Symposium, Vol. 3, April 1960.

21. R. D. Collins, Jr., and W. H. Kinard, The Dependency of Penetration on the Momentum per Unit Area of the Impacting Projectile and the Resistance of Materials to Penetration, NASA TN D-238, May 1960.

22. R. L. Fox and R. R. Eaton, Two-Dimensional Modeling of the Flow of Blast Debris from Underground Nuclear Tests, SLA-73-0985, Sandia Laboratories, Albuquerque, New Mexico, October 1973.

23. P. M. Morse and H. Feshbach, Methods of Theoretical Physics, Vol. 1, McGraw Hill Book Company, New York 1953, pp. 116, 272.

DISTRIBUTION:

1100 C. D. Broyles
Attn: 1110 L. R. Hill
1111 W. D. Weart
1130 H. E. Viney
1133 R. D. Statler
1500 R. L. Peurifoy
Attn: 1540 T. B. Lane
1541 S. W. Key
1542 T. G. Priddy
4700 D. B. Shuster
Attn: 4730 R. G. Clem
4750 J. M. Wiesen
5000 A. Narath
5100 J. K. Galt
Attn: 5130 G. A. Samara
5131 L. W. Davison
5132 P. M. Richards
5160 W. Herrmann
Attn: 5162 L. D. Bertholf
5163 D. E. Munson
5166 A. J. Chabai
5167 B. M. Butcher
5200 E. H. Beckner
5600 A. Y. Pope
Attn: 5620 R. C. Maydew
5623 J. E. Deveney
5640 K. J. Touryan
Attn: 5640 F. G. Blottner
5641 T. A. Green
5641 R. L. Fox (5)
5642 R. A. Hill
5642 D. P. Aeschliman (20)
5642 A. J. Mulac (5)
5644 J. K. Cole
5644 R. R. Eaton (5)
5645 C. W. Peterson
5700 J. H. Scott
Attn: 5710 G. F. Brandvold
5716 W. N. Caudle
5718 M. M. Newsom
5720 M. L. Kramm
5725 D. J. Ragali
5730 H. Stoller
5800 L. M. Berry
8100 L. Gutierrez
8110 A. N. Blackwell
8115 D. L. Hartley
8300 B. F. Murphey
Attn: 8310 R. H. Meinken
8320 T. S. Gold
8330 G. W. Anderson

9300 L. A. Hopkins
Attn: 9320 M. Cowan, Jr.
9324 M. J. Forrestal
9330 A. J. Clark
9331 P. H. Adams
9332 M. McWhirter
9333 J. V. Otts
9334 J. L. Mortley
9340 W. E. Caldes
9342 D. R. Schafer
3141 L. S. Ostrander (5)
3151 W. F. Carstens (3)
For ERDA/TIC (Unlimited Release)
8266 E. A. Aas (2)